Chemical Size Effect on the Magnetic and Electrical Properties in the (Tb 1− x Eu x)MnO 3 (0 ≤ x ≤ 1.0) System

7 AUTHORS, INCLUDING:

Ren-Shyan Liu
Taipei Veterans General Hospital
592 PUBLICATIONS **7,334** CITATIONS

Chun Chuen Yang
Chung Yuan Christian University
40 PUBLICATIONS **370** CITATIONS

Wen-Hsien Li
National Central University
268 PUBLICATIONS **3,573** CITATIONS

Chemical Size Effect on the Magnetic and Electrical Properties in the (Tb$_{1-x}$Eu$_x$)MnO$_3$ (0 ≤ x ≤ 1.0) System

T. S. Chan,† R. S. Liu,*,† C. C. Yang,‡ W.-H. Li,§ Y. H. Lien,$^{\parallel}$ C. Y. Huang,$^{\perp}$ and J.-F. Lee$^{\#}$

Department of Chemistry and Center for Nano Storage Research, National Taiwan University, Taipei 106, Taiwan, Institute of Physics, Academia Sinica, Taipei 115, Taiwan, Department of Physics, National Central University, Chung-Li 320, Institute of Materials Manufacturing, Chinese Culture University, Taipei 111, Taiwan, Institute of Optoelectronic Science and Technology, National Taiwan Normal University, Taipei 106, Taiwan, and National Synchrotron Radiation Research Center, Hsinchu 300, Taiwan

The effect of isovalent chemical substitution of Eu^{3+} into the Tb^{3+} sites on the magnetic and electrical properties of (Tb$_{1-x}$Eu$_x$)MnO$_3$ (0 ≤ x ≤ 1.0) system has been investigated. The orthorhombic structure with space group *Pbnm* is observed in this series of materials. An increase in Mn−O bond distance with increasing Eu content leads to improvement in the overlap between the Mn 3d and O 2p orbital thereby causing a decrease in activation energy and resistivity. Moreover, as the Eu content increases, the effective moments (μ_{eff}) are reduced linearly and an exchange coupling is observed in Tb−Tb, Tb−Eu, and Eu−Eu complexes for x = 0.1 and 0.3 samples. Both these features can be related to the substitution of bigger Eu^{3+} ions replacing the original Tb−Tb coupling.

Introduction

Magnetoelectric (ME) effect, that is, controlling the electric polarization by a magnetic field or inversely the magnetization by an electric field, has received renewed interest in recent years.[1] However, the magnitude of the ME effect of materials reported in the literature remains too small for actual technological applications. The only way of achieving a noticeable improvement in ME response is to make use of strong internal electromagnetic fields by finding components with a large dielectric or magnetic susceptibility. The largest dielectric coefficients are found in ferroelectrics, while ferromagnets exhibit the largest magnetic permeability. Therefore, recent discovery of anomalously large interplay between ferroelectric and magnetism in many multiferroic materials has accelerated much interest, for example, the kagomé-staicase compound Ni$_3$V$_2$O$_8$,[2] rare-earth manganites like orthorhombic TbMnO$_3$,[3] hexagonal YMnO$_3$,[4] or pervoskites like TbMn$_2$O$_5$[5] and Bi$_2$-NiMnO$_6$.[6]

Among the orthorhombic perovskite manganites, TbMnO$_3$ is one of the latter series of RMnO$_3$ (R is a trivalent rare earth ion) studied. It show an incommensurate sinusoidal spin order with $q_{\text{Mn}} \sim 0.295$ below $T_{\text{N}} \sim 41$ K having spins oriented along the [010] direction. The magnetic structure of the Mn^{3+} moments for this compound has been identified.[7−12] In addition, recently the development of ferroelectricity in TbMnO$_3$ has been connected to the breaking of magnetic inversion symmetry rather than to the formation of an incommensurate magnetic structure.[12,13] On the other hand, the doping of TbMnO$_3$ has also been reported in polycrystalline (Tb$_{1-x}$Ca$_x$)MnO$_3$,[14] (Tb$_{1-x}$Na$_x$)-

MnO$_3$,[15,16] and single-crystal (Tb$_{1-x}$Gd$_x$)MnO$_3$[17] systems. However, there are very few published reports on the evolution of the magnetic and transport properties in the (Tb$_{1-x}$Eu$_x$)MnO$_3$ system.

Here, we demonstrate the synthesis and chemical size effect (by the substitution of isovalent bigger Eu^{3+} ions into the smaller Tb^{3+} sites, corresponding to the internal pressure) in the (Tb$_{1-x}$Eu$_x$)MnO$_3$ (0 ≤ x ≤ 1.0) system. The detailed crystallographic behavior for these materials was studied by a combination of X-ray powder diffraction and Raman spectroscopy, which will be discussed. The electronic structure from X-ray absorption spectra (XAS) measurements at the Mn K-edge and magnetic properties are also reported.

Experimental Section

The polycrystalline samples of (Tb$_{1-x}$Eu$_x$)MnO$_3$ (0 ≤ x ≤ 1.0) were synthesized by conventional solid-state reaction. Stoichiometric mixtures of high-purity powders of Tb$_4$O$_7$, Eu$_2$O$_3$, and MnCO$_3$ were sintered in air at 1450 °C for 24 h. X-ray diffraction (XRD) measurements were carried out on a SCINTAG (X1) diffractometer (Cu Kα radiation, $\lambda = 1.5406$ Å) at 40 kV and 30 mA. The GSAS program[18] was used for the Rietveld refinements to obtain information on the crystal structures of (Tb$_{1-x}$Eu$_x$)MnO$_3$. Raman spectra were recorded on a Jobin Yvon T64000 spectrometer in the backscattering mode, employing a 514.5-nm line from an Ar$^+$ laser as the excitation line with an input power of 0.5 mW (at the focus spot, 2∼3 μm in diameter) directed onto the sample. A nitrogen cryostat pump was used to control the sample temperature, and sufficient time was allowed for each temperature change.

The Mn K-edge X-ray absorption near-edge structure (XANES) was recorded in transmission mode for synthesized powder mounted on Scotch tape, at a BL17C Wiggler beamline by using a double-crystal Si(111) monochromator. The X-ray high harmonic was rejected by mirrors. The ion chambers used for measuring the incident (I_0) and transmitted (I) beam intensities

* To whom correspondence should be addressed. E-mail: rsliu@ntu.edu.tw.
† National Taiwan University.
‡ Academia Sinica.
§ National Central University.
$^{\parallel}$ Chinese Culture University.
$^{\perp}$ National Taiwan Normal University.
$^{\#}$ National Synchrotron Radiation Research Center.

Chemical Size Effect on (Tb$_{1-x}$Eu$_x$)MnO$_3$ System

J. Phys. Chem. B, Vol. 111, No. 9, 2007 **2263**
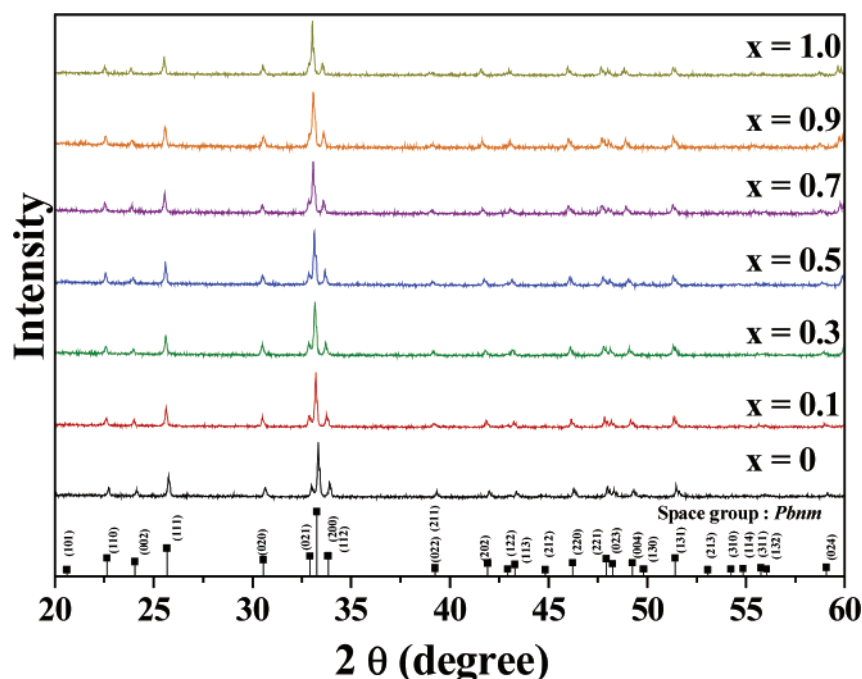
Figure 1. Powder XRD patterns of (Tb$_{1-x}$Eu$_x$)MnO$_3$ (0 ≤ x ≤ 1.0).

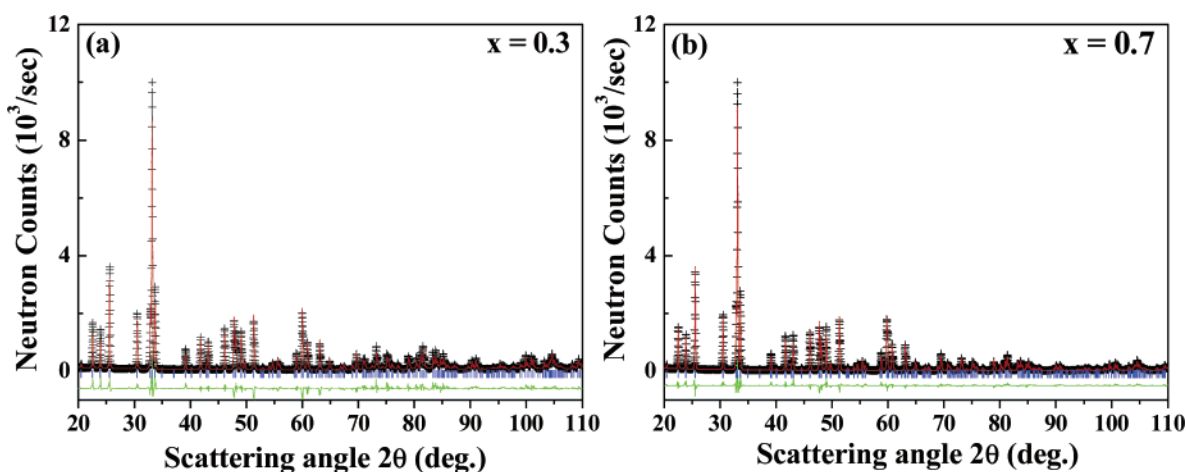**Figure 2.** Observed (crosses), calculated (solid line), and differences (bottom) NPD Rietveld profiles of (Tb$_{1-x}$Eu$_x$)MnO$_3$ for (a) x = 0.3 and (b) x = 0.7 at 300 K. Bragg reflections are indicated by tick mark.

were filled with a mixture of N$_2$ and H$_2$ gases and a mixture of N$_2$ and Ar gases, respectively. Energy calibration was carried out by using the first inflection point of the Mn K-edge (6539 eV) absorption spectrum of Mn metal foil as a reference. Reference spectra were simultaneously collected for each in-situ spectrum by using Mn metal foils.

Resistivity measurements were performed by the conventional four-probe technique. Magnetic susceptibilities were measured between 5 and 350 K by a commercial Quantum Design (PPMS) magnetometer with an ac experimental setup.

Results and Discussion

Powder XRD patterns of (Tb$_{1-x}$Eu$_x$)MnO$_3$ (0 ≤ x ≤ 1.0) samples are shown in Figure 1. Each composition of the series was found to be single phase. The observed peaks can be indexed on the basis of an orthorhombic unit cell (space group: *Pbnm*). This is one of the most common distorted structures derived from the cubic perovskites. Figure 2 a and 2b shows experimental, calculated, and difference in XRD patterns of (Tb$_{1-x}$Eu$_x$)MnO$_3$ (x = 0.3, 0.7) at 300 K with λ =

1.5406 Å. The final structural parameters are given in Table 1 and selected bond length and angles are listed in Table 2. As seen in Figure 3, the lattice constants (a and c) increase as the Eu (x) content increases. However, there was hardly any variation in the b parameter as compared to that of a and c. This can be attributed to the tilting scheme of MnO$_6$ octahedral in *Pbnm* perovskites of the type a$^-$ a$^-$ c$^+$ in Glazer's nomenclature,[19] in which the distortion is driven by a difference in the R^{3+} sizes causing b to almost remain unchanged. Moreover, an increase in cell volume with increasing x was also found. The increase in the cell volume can be accounted as a manifestation of the substitution of bigger size Eu^{3+} ion [1.120 Å for CN (coordination number) = 9] as compared to the smaller Tb^{3+} ions (1.095 Å for CN = 9).[20]

Figure 4 shows the dependence of the tolerance factor and Mn−O bond distances on the effective ionic radius of the A-site-($<r_A>$). It was found that the enlargement of the Mn−O (along each direction of the MnO$_6$ octahedra) bond distance is consistent with an increase in the cell volume. Moreover, an increase in the tolerance factor (t_{factor}) with increasing Eu doping

TABLE 1: Refined Atomic Positions, Isotropic Thermal Factors, Occupancies, and Reliability Factors of $(Tb_{1-x}Eu_x)MnO_3$ in Orthorhombic *Pbnm* Space Group from X-ray Diffraction Data at 300 K^a
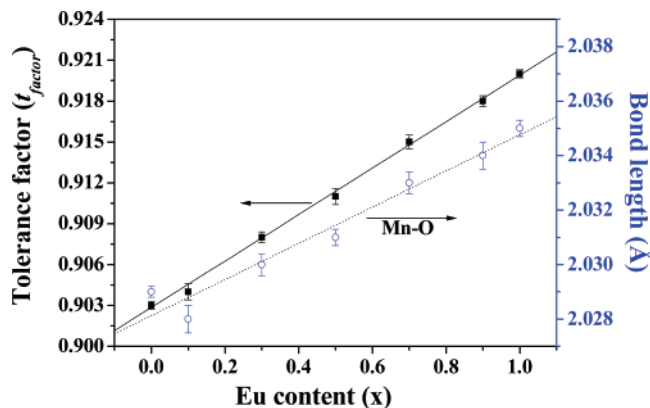
no.	$x = 0$	$x = 0.1$	$x = 0.3$	$x = 0.5$	$x = 0.7$	$x = 0.9$	$x = 1.0$
a/Å	5.2963(2)	5.3013(2)	5.3133(3)	5.3192(2)	5.3261(1)	5.3333(1)	5.3379(1)
b/Å	5.8480(2)	5.8499(2)	5.8529(3)	5.8554(2)	5.8518(1)	5.8506(3)	5.8483(2)
c/Å	7.3967(2)	7.4034(2)	7.4184(3)	7.4267(2)	7.4353(2)	7.4451(2)	7.4519(2)
V/Å^3	229.10(2)	229.59(2)	229.89(2)	231.31(2)	231.74(1)	232.31(1)	232.63(1)
s	0.0990	0.0984	0.0967	0.0960	0.0941	0.0925	0.0913
Tb : x	0.9828(5)	0.9819(2)	0.9823(2)	0.9826(3)	0.9853(4)	0.9842(4)	0.9843(2)
4c (x y 1/4)							
Tb : y	0.0828(2)	0.0817(1)	0.0817(1)	0.0807(1)	0.0825(4)	0.0785(2)	0.0775(2)
Uiso (Å^2)	2.10(4)	1.94(3)	2.14(5)	1.86(3)	2.23(3)	2.40(3)	2.16(3)
occupancy (Tb)	1	0.9	0.7	0.5	0.2	0.1	0
occupancy (Eu)	0	0.1	0.3	0.5	0.7	0.9	1
Mn	(1/2 0 0)	(1/2 0 0)	(1/2 0 0)	(1/2 0 0)	(1/2 0 0)	(1/2 0 0)	(1/2 0 0)
4 b (1/2 0 0)							
Uiso (Å^2)	2.59(7)	2.25(6)	1.85(6)	1.93(5)	2.27(7)	2.39(5)	1.71(5)
O(1) : x	0.1068(2)	0.1140(1)	0.1147(1)	0.1173(1)	0.0970(1)	0.1146(1)	0.0972(1)
4c (x y 1/4)							
O(1) : y	0.4553(2)	0.4575(1)	0.4595(1)	0.4642(1)	0.4717(1)	0.4675(1)	0.4694(1)
Uiso (Å^2)	4.87(3)	3.91(3)	4.56(3)	4.26(3)	3.89(2)	4.12(2)	4.84(2)
O(2) : x	0.7053(1)	0.7090(1)	0.7073(1)	0.7084(1)	0.7054(1)	0.7124(1)	0.7054(1)
8d(x y z)							
O(2) : y	0.3278(1)	0.3330(1)	0.3298(1)	0.3293(1)	0.3309(1)	0.3197(8)	0.3290(1)
O(2) : z	0.0528(8)	0.0578(7)	0.0588(6)	0.0590(7)	0.0479(7)	0.0462(7)	0.0488(8)
Uiso (Å^2)	4.66(2)	3.96(2)	4.33(2)	4.38(2)	4.35(4)	4.42(2)	3.94(2)
R_p%/R_{wp}%	8.80/11.52	7.41/9.72	8.21/10.32	7.49/9.68	7.57/10.21	7.73/9.99	8.64/11.07
χ^2	2.66	1.91	2.42	1.81	1.61	1.69	2.04

^{a} The strain parameter is defined as $s = 2(b - a)/(a + b)$.

TABLE 2: Selected Tb−O, Mn−O Distances (Å) and Mn−O−Mn Angles for the Refinements of $(Tb_{1-x}Eu_x)MnO_3$ in Orthorhombic *Pbnm* Space Group from X-ray Diffraction Data at 300 K^a

no.	$x = 0$	$x = 0.1$	$x = 0.3$	$x = 0.5$	$x = 0.7$	$x = 0.9$	$x = 1.0$
Tb(Eu)−O(1) average × 2	2.286(8)	2.289(7)	2.293(5)	2.296(7)	2.308(6)	2.346(6)	2.769(6)
Tb(Eu)−O(2) average × 6	2.472(7)	2.478(5)	2.481(4)	2.482(6)	2.486(5)	2.501(6)	2.521(6)
Mn−O average × 6	2.029(2)	2.028(5)	2.030(4)	2.031(3)	2.033(4)	2.035(5)	2.038(3)
Mn−O−Mn	180.0(0)	179.97(0)	180.0(0)	180.0(0)	179.98(0)	180.0(0)	180.0(0)
C (emu K/g)	0.0511(6)	0.0595(5)	0.0441(3)	0.0390(2)	0.0317(1)	0.0264(3)	0.0214(3)
T_θ (K)	−13.8(3)	−9.0(2)	−6.3(2)	−14.0(3)	−26.5(2)	−67(1)	−89(2)
μ_{eff} (fit) (μB)	10.35(6)	11.14(5)	9.57(3)	8.98(2)	8.08(1)	7.34(5)	6.61(5)
fit range	50−350 K	50−350 K	50−350 K	50−350 K	55−350 K	55−300 K	55−350 K

^{a} Some physical parameters obtained from the Curie−Weiss fits are also given.
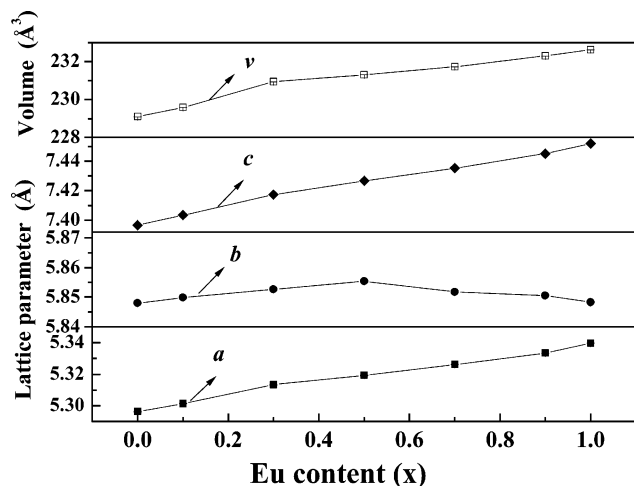
Figure 3. The lattice parameters and unit cell volume as a function of Eu concentration. Error bars are smaller than symbol size.

Figure 4. Tolerance factors and Mn−O bond distances as a function of Eu concentration of $(Tb_{1-x}Eu_x)MnO_3$ ($0 \leq x \leq 1.0$).

was found. The tolerance factor is defined as $(r_A + r_O)/\sqrt{2}(r_B + r_O)$,[21] where r_A, r_B, and r_O are the ionic radii of the A, B cations and oxygen in the perovskite ABO_3 structure, respectively. The $t_{factor} = 1$ for the compound with an ideal perovskite structure. For $t_{factor} < 1$, the strain within the compound is increased. Therefore, increase in the t_{factor} from 0.903 (for $x =$

$0-0.920$ for $x = 1.0$) with the addition of Eu gives rise to the release of the strain from $(Tb_{1-x}Eu_x)MnO_3$ ($0 \leq x \leq 1.0$) system. Furthermore, the spontaneous orthorhombic strain, defined as $s = 2(b - a)/(a + b)$, which also is a measure of the distortion of the octahedral, increases as a consequence of the octahedral tilting.[22] As seen in Table 1, the s value (0.099) of $TbMnO_3$ is in agreement with the early report by Alonso et al. ($s = 0.098$),[23] who also showed the increase of the Jahn−Teller (JT) effect, which is observed from La to Tb. In our case, the s value
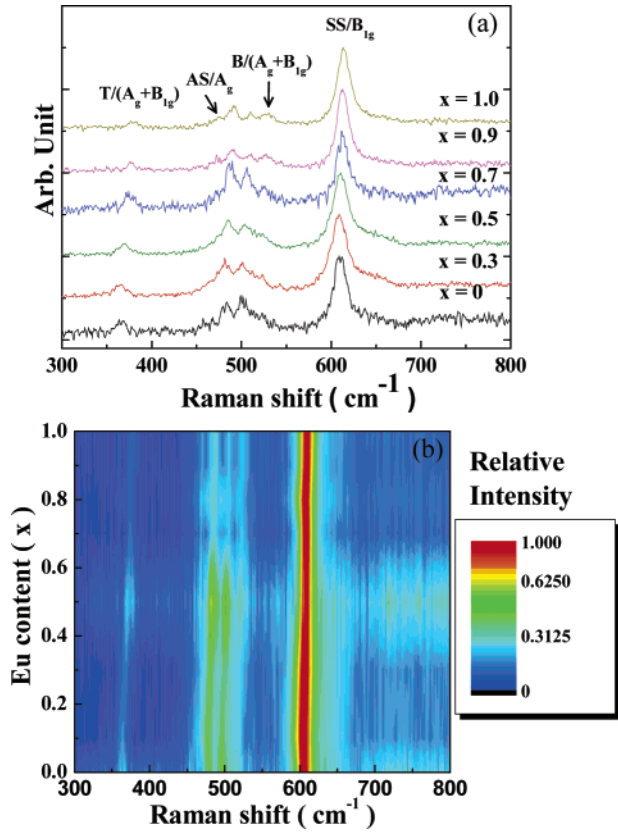
Chemical Size Effect on $(Tb_{1-x}Eu_x)MnO_3$ System

J. Phys. Chem. B, Vol. 111, No. 9, 2007 **2265**

Figure 5. (a, b) Measured frequency range (300−800 cm⁻¹) of Raman spectra of $(Tb_{1-x}Eu_x)MnO_3$ ($0 \leq x \leq 1.0$) at 300 K.

decreases with increasing Eu content, which indicates the reduction in the octahedral distortion and JT effect.

Raman scattering is an excellent tool to study crystal symmetry and its dependence on doping. Hence, it will be interesting to study the Raman spectra of the $(Tb_{1-x}Eu_x)MnO_3$ ($0 \leq x \leq 1.0$) system to get more insight into the order−disorder and the local distortion present in the samples. The vibration modes allowed in the RMnO₃ compounds have been identified,[24−26] and it is well-known that for $(Tb_{1-x}Eu_x)MnO_3$ the *Pbnm* symmetry allows 24 active Raman modes ($7A_g + 7B_{1g} + 5B_{2g} + 5B_{3g}$). Martín-Carrón[25] et al. labeled five observed Raman modes of RMnO₃, namely, R for rare-earth ion mode at ∼250 cm⁻¹; T for the tilt, A_g mode in-between 280∼370 cm⁻¹; AS for asymmetric stretch A_g mode at around 480 cm⁻¹; *B* for the bending $A_g + B_{1g}$ between 420∼530 cm⁻¹; and SS (symmetric stretch), B_{1g}, around 610 cm⁻¹ notation. Recently, Iliev[26] et al. reported a series of Raman experiments on the single-crystal RMnO₃. They pointed out the correction for some normal modes of Martín-Carrón notation. In our studies, we have used Martín-Carrón's notation with Iliev's corrections. The measured frequency range (300−800 cm⁻¹) of the Raman spectra of $(Tb_{1-x}Eu_x)MnO_3$ ($0 \leq x \leq 1.0$) is plotted as shown in Figure 5a and 5b. The fitting parameters are plotted and listed in Figure 6 and Table 3, respectively. For $x = 0$ sample, it was found that the sample showed four features labeled as T, AS, B, and SS at around 379, 489, 528, and 614 cm⁻¹, respectively.[25] One of the second-order Raman scattering features was also observed, which was mainly due to the oxygen vibration mode[27] at 650 cm⁻¹ consistent with the previous report.[25] Moreover, it is known that the T, AS, B, and SS modes are related to Mn−O(1)−Mn angle, <Mn−O> length, <Mn−O> length, and <Tb−O(1)> length, respectively. As seen in Figure 6, the overall spectra show that there is a reduced Raman shift with

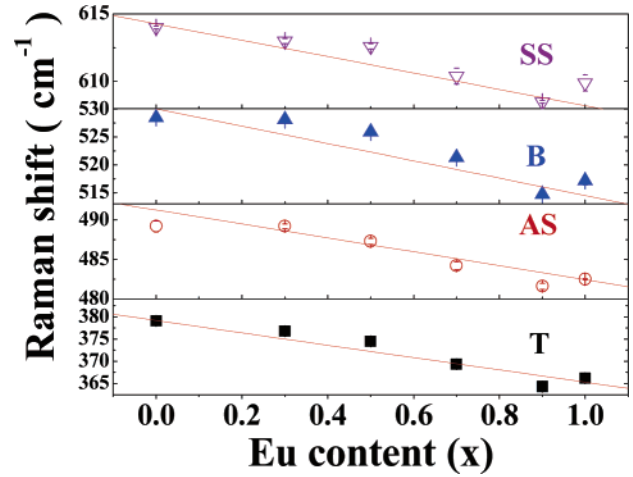**Figure 6.** Raman shift as a function of Eu concentration of $(Tb_{1-x}Eu_x)MnO_3$ ($0 \leq x \leq 1.0$) with fitted peak position.

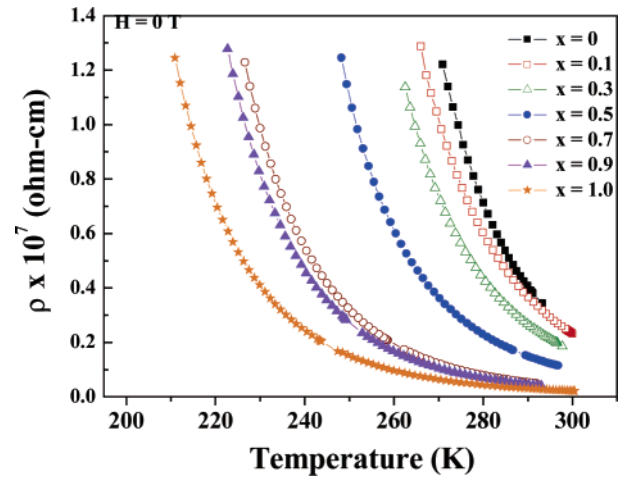**Figure 7.** Temperature dependence of resistivity (ρ) of $(Tb_{1-x}Eu_x)MnO_3$ ($0 \leq x \leq 1.0$).

TABLE 3: Raman Shifts Identified of $(Tb_{1-x}Eu_x)MnO_3$ ($0 \leq x \leq 1.0$)

no.	T (cm⁻¹)	AS (cm⁻¹)	B (cm⁻¹)	SS (cm⁻¹)
0	379.1(1)	489.2(7)	528.5(3)	614.0(1)
0.3	376.8(6)	489.2(3)	528.1(5)	613.0(2)
0.5	374.5(5)	487.3(4)	525.9(6)	612.6(2)
0.7	369.3(1)	484.2(5)	521.3(3)	610.4(6)
0.9	364.3(3)	481.6(4)	514.7(2)	608.5(1)
1.0	366.2(2)	482.5(1)	517.2(8)	609.9(6)

substitution of Tb by Eu. This can be explained by assuming the decreased lattice distortion and increased bond lengths, which reasonably results in a twofold effect of reduction in Raman intensity as well as a shift in Raman frequencies. This is also in agreement with the sketch shown in Figure 4.

Figure 7 shows the temperature dependence of resistivity of $(Tb_{1-x}Eu_x)MnO_3$ ($0 \leq x \leq 1.0$) compounds in the absence of magnetic field. All samples show an insulator behavior over the whole temperature range. On the basis of the small polarons model arising from the Jahn−Teller distortion of strong lattice−electron interaction, the $E + W$ values (E, the energy required to produce intrinsic carriers; W, the polarons' formation energy) can be calculated.[28] Figure 8 shows the log ρ/T versus $1/T$ curves for $(Tb_{1-x}Eu_x)MnO_3$ ($0 \leq x \leq 1.0$) samples. The plot of activation energy ($E + W$) as a function of x is also shown in the inset. A decrease in $E + W$ values from 78.8 meV ($x = 0$) to 50.6 meV ($x = 1.0$) is observed which indicates a decrease
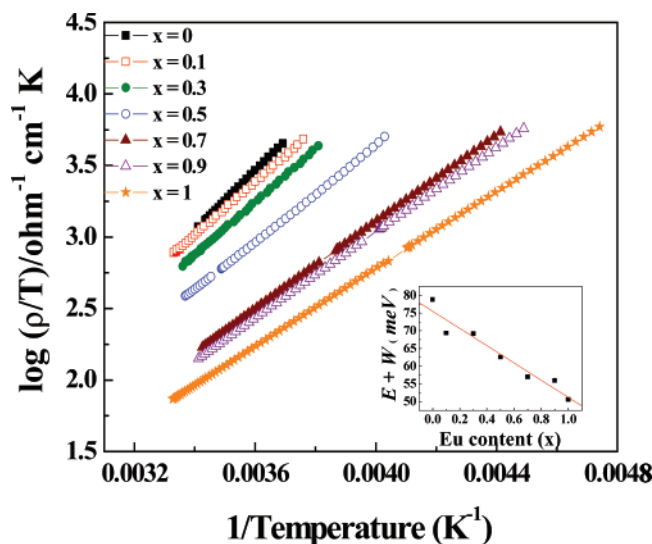
Figure 8. Log ρ/T vs $1/T$ curves of $(Tb_{1-x}Eu_x)MnO_3$ ($0 \leq x \leq 1.0$). The activation energy ($E + W$) as a function of x is also shown in the inset.
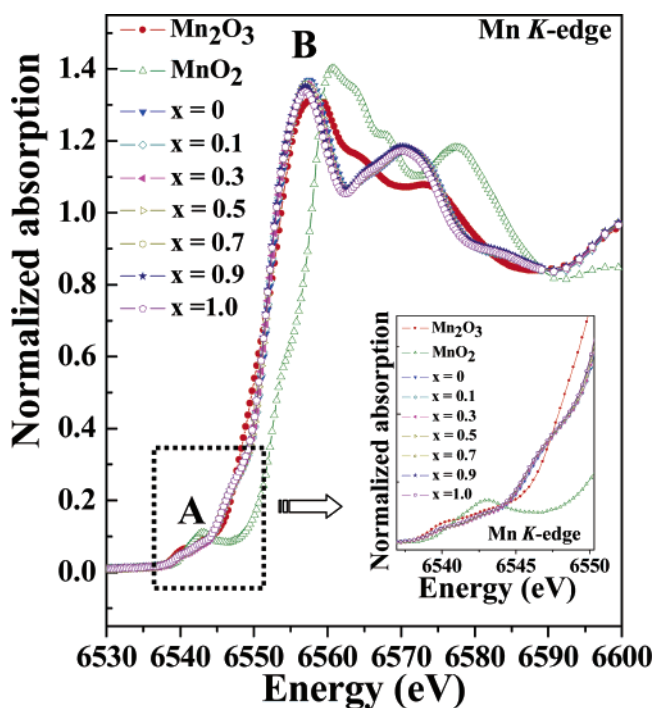

Figure 9. Mn K-edge XANES spectra of $(Tb_{1-x}Eu_x)MnO_3$ along with two standards of Mn_2O_3 (Mn^{3+}) and MnO_2 (Mn^{4+}) for comparison.

in activation energy and resistivity with increasing Eu doping in $(Tb_{1-x}Eu_x)MnO_3$.

X-ray absorption spectroscopy (XAS) has been employed to probe the electronic and local structure of transition-metal ions. It is already known that the absorption features of the transition-metal K-edge XAS provide useful structural information, such as oxidation state of chemical species, their site symmetries, and covalent bond strength.[29–33] We have studied whether there is any change in the formal Mn valency of $(Tb_{1-x}Eu_x)MnO_3$ on account of substitution of Tb by Eu. The Mn K-edge XANES spectra of $(Tb_{1-x}Eu_x)MnO_3$ are shown in Figure 9 along with two standards, Mn_2O_3 (Mn^{3+}) and MnO_2 (Mn^{4+}) used for comparison. The weak preedge peak, labeled A in the figure, emerges from the 1s $\rightarrow$ 3d transition which is due to pure electric quadrupole coupling or 3d−4p orbital mixing arising from the noncentrosymmetric environment of the slightly distorted
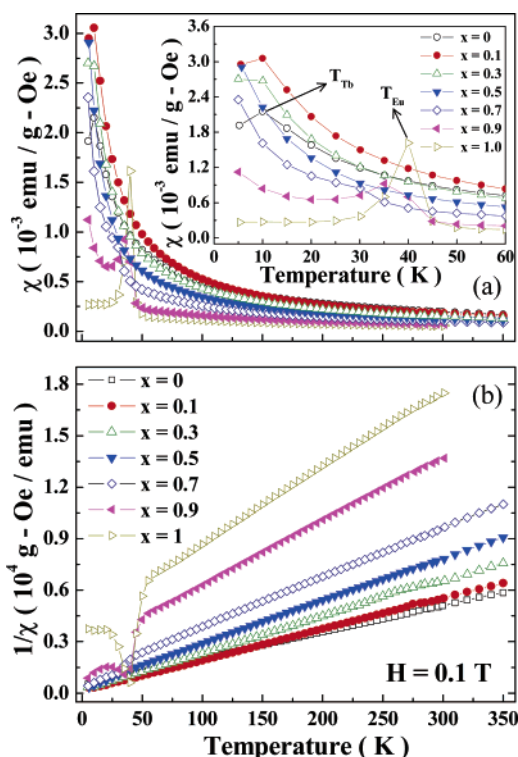

Figure 10. Temperature dependence of (a) the magnetic susceptibility (χ) and (b) reciprocal magnetic susceptibility of $(Tb_{1-x}Eu_x)MnO_3$ ($0 \leq x \leq 1.0$) at magnetic field 0.1 T.

octahedral site in the orthorhombic *Pbnm* space group. The main absorption features labeled B in Figure 9 can be ascribed to the pure dipole-allowed 1s $\rightarrow$ 4p transition. As Eu content increases, the Mn K-edge XANES spectrum shows systematic changes in the shape and intensity of preedge peaks. Especially noteworthy is that peak B does not show a clear shift to higher energy values. The energy position and shape of these absorption features are very similar to those of Mn_2O_3 standard compounds. This indicates that the valency of Mn ions in $(Tb_{1-x}Eu_x)MnO_3$ remains nearly 3+ with increasing Eu content. Similar results have also been found from the refined structure parameters calculated by bond valence sum.[34]

The effect of Eu doping on the magnetic properties of $(Tb_{1-x}Eu_x)MnO_3$ is also studied. Figure 10a and b depicts the χ versus T and $1/\chi$ versus temperature curves for $(Tb_{1-x}Eu_x)MnO_3$ ($0 \leq x \leq 1.0$) at 0.1 T. All $1/\chi$ versus temperature data can be fitted to a straight line at high-temperature regime as shown in Figure 10b, which reveals that these series of compounds follow Curie−Weiss behavior ($\chi = C/(T - T_\theta)$). The fit results are summarized in Table 2. At low-temperature regime, a sharp peak is clearly observed at $x = 1.0$, 0.9, and 0.7 samples in both Figure 10a and b, which originated at Eu magnetic ordering. The Néel temperature T_{Eu} was found to be about 40 K and shifted to lower temperature with decreasing x, which can be associated with the dilution effect from Tb ions. On the other hand, the anomaly comes from Tb magnetic ordering also found at 10 K (T_{Tb}) for low Eu concentration in the sample ($x = 0$, 0.1, and 0.3) as shown in the inset of Figure 10a. Both T_{Tb} at 10 K ($x = 0$) and T_{Eu} at 40 K ($x = 1.0$) are in good agreement with the earlier reported values of $TbMnO_3$ by Blasco et al.[14] and $EuMnO_{3.02}$ by Troyanchuk et al.,[35] respectively. The temperature dependence of effective moment and T_θ are plotted in Figure 11. Obviously, the effective moments (μ_{eff}) decrease with increasing x, which is simply due to the replacement of nonmagnetic Eu^{3+} ions by Tb^+ ions. Moreover, the bigger doped
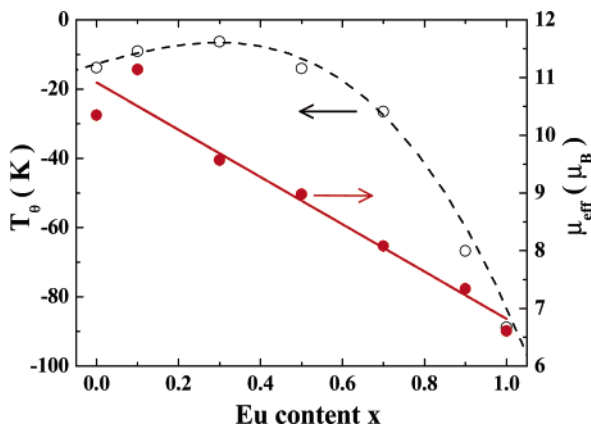
Chemical Size Effect on (Tb$_{1-x}$Eu$_x$)MnO$_3$ System

J. Phys. Chem. B, Vol. 111, No. 9, 2007 **2267**

Figure 11. Néel temperature (T_N) and Tb moment (μ_B) as a function of Eu concentration of (Tb$_{1-x}$Eu$_x$)MnO$_3$ ($0 \leq x \leq 1.0$).
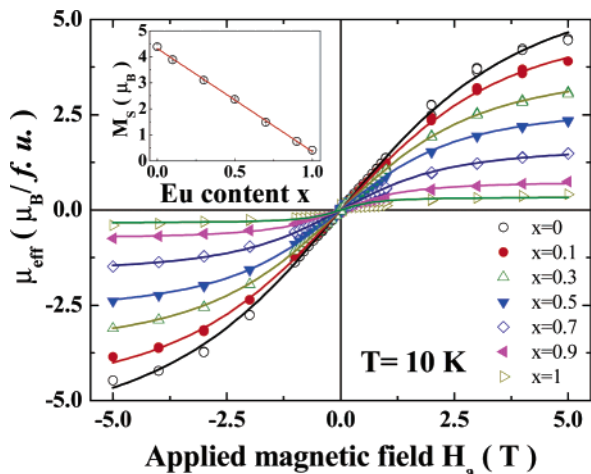

Figure 12. Magnetic hysteresis curves and Langevan of (Tb$_{1-x}$Eu$_x$)MnO$_3$ ($0 \leq x \leq 1.0$) at 300 K. The fitted effect moment (μ_B) as a function of x is also shown in the inset.

Eu^{3+} ion enlarges the separation of Tb ions, which replaced the exchange coupling from major interaction between Tb–Tb ions to Eu–Eu one. The T_θ and μ_{eff} anomalies observed for x = 0.1 and 0.3 samples suggest that the observed magnetism comes from complex Tb–Tb, Tb–Eu, and Eu–Eu exchange coupling. In addition, Figure 12 shows magnetic hysteretic curves of (Tb$_{1-x}$Eu$_x$)MnO$_3$ ($0 \leq x \leq 1.0$) at 10 K by applying Langevin function[36] ($M = M_S[\coth(x) - 1/x]$, $x = \mu_B H/k_B T$) to fit the magnetization data. The saturation moment M_S is reduced linearly as increasing x (shown in the inset of Figure 12), which is also due to replacement of Tb by Eu.

Conclusions

The structure and magnetic properties of (Tb$_{1-x}$Eu$_x$)MnO$_3$ samples have been studied by means of X-ray diffraction study and ac susceptibility. With the increase in the Eu content, both the tolerance factor (t_{factor}) and Mn–O bond distance was increased, which leads to reduction in the octahedral distortion and JT effect. These results were supported by Raman spectroscopic measurement, which found reduced Raman intensity and shift in the Raman frequencies. The Eu-rich samples present small structural distortion which is responsible for the reduced insulator behavior of series of samples and influence on the magnetic properties.

References and Notes

(1) Fiebig, M. *J. Phys. D: Appl. Phys.* **2005**, *38*, R123.
(2) Lawes, G.; Harris, A. B.; Kimura, T.; Rogado, N.; Cava, R. J.; Aharony, A.; Entin-Wohlman, O.; Yildirim, T.; Kenzelmann, M.; Broholm, C.; Ramirez, A. P. *Phys. Rev. Lett.* **2005**, *95*, 087205.
(3) Kimura, T.; Koto, T.; Shintani, H.; Ishizaka, K.; Arima, T.; Tokura, Y. *Euture* **2003**, *426*, 55.
(4) Van Aken, B. B.; Palstra, T. T. M.; Filippetti, A.; Spaldin, N. A. *Eut. Mater.* **2004**, *3*, 164.
(5) Hur, N.; Park, S.; Sharma, P. A.; Ahn, J. S.; Guha, S.; Cheong, S.-W. *Nature* **2004**, *429*, 392.
(6) Azuma, M.; Takata, K.; Saito, T.; Ishiwata, S.; Shimakawa, Y.; Takano, M. *J. Am. Chem. Soc.* **2005**, *127*, 8889.
(7) Quezel, S.; Tcheou, F.; Rossat-Mignod, J.; Quezel, G.; Roudaut, E. *Physica B+C* **1977** *86−88.*, 916.
(8) Blasco, J.; Ritter, C.; Garcia, J.; de Teresa, J. M.; Parez-Cacho, J.; Ibarra, M. R. *Phys. Rev. B* **2000**, *62*, 5609.
(9) Kajimoto, R.; Yoshizawa, H.; Shintani, H.; Kimura, T.; Tokura, Y. *Phys. Rev. B* **2004**, *70*, 012401.
(10) Munoz, M.; Casais, T.; Alonso, J. A.; Martinez-lopez, M. J.; Martinez, J. L. Fernandez-Diaz, M. T. *Inorg. Chem.* **2001**, *40*, 1020.
(11) Vajk, O. P.; Kenzelmann, M. Lynn, J. W.; Kim, S. B.; Cheong, S.-W. *Phys. Rev. Lett.* **2005**, *94*, 87601.
(12) Kenzelmann, M.; Harris, A. B.; Jonas, S.; Broholm, C.; Schefer, J.; Kim, S. B.; Zhang, C. L.; Cheong, S.-W. Vajk, O. P.; Lynn, J. W. *Phys. Rev. Lett.* **2005**, *95*, 87206−1.
(13) Lawes, G.; Harris, A. B.; Kimura, T.; Rogado, N.; Cava, R. J.; Aharony, A.; Entin-Wohlman, O.; Yildirm, T.; Kenzelmann, M.; Broholm, C.; Ramirez, A. P. *Phys. Rev. Lett.* **2005**, *95*, 087205(R).
(14) Blasco, J.; Ritter, C.; García, J.; Teresa, J. M.; Perez-Cacho, J.; Ibarra, M. R. *Phys. Rev. B* **2000**, *62*, 5609.
(15) Yang, C. C.; Chung, M. K.; Chan, T. S.; Liu, R. S.; Lien, Y. H.; Huang, C. Y.; Chan, Y. Y. Yao, Y. D.; Lynn, J. W. *Phys. Rev. B.* **2006**, *74* 094409-1.
(16) Chan, T. S.; Liu, R. S.; Lien, Y. H.; Yang, C. C.; Huang, C. Y.; Lin, J. G. *IEEE Trans. Magn.* **2005**, *41*, 2751.
(17) Goto, T.; Yamasaki, Y.; WataEube, H.; Kimura, T.; Tokura, Y. *Phys. Rev. B* **2005**, *72*, 220403.
(18) Larson, A. C.; Von Dreele, R.B.; *Generalized Structure Analysis System (GSAS)*; Los Alamos National Laborator Report LAUR 86-748; 1994.
(19) Giazer, A. M. *Acta Crystallogr., Sect. B* **1972**, *28*, 3384.
(20) Shannon, R. D. *Acta Crystallogr., Sect. A* **1976**, *32*, 751.
(21) Geller, S. J. *J. Chem. Phys.* **1956**, *24*, 1236.
(22) Woodward, P. M.; Vogt, T.; Cox, D. E.; Arulraj, A.; Rao, C. N. R.; Karen, P.; Cheetharm, A. K. *Chem. Mater.* **1998**, *10*, 3652.
(23) Alonso, J. A.; Martinez-Lope, M. J.; Casais. M. T.; FerEundez-Diaz, M. T. *Inorg. Chem.* **2000**, *39*, 917.
(24) Abrashev, M. V.; Bäckström, J.; Börjesson, L.; Popov, V. N.; Chakalov, R. A.; Kolev, N.; Meng, R.-L.; Iliev, M. N. *Phys. Rev. B* **2002**, *65*, 184301−1.
(25) Martín-Carrón, L.; Andrés, A. D; Martínez-Lope, M. J.; Casais, M. T.; Alonso J. A. *Phys. Rev. B* **2002**, *66*, 174303.
(26) Iliev, M. N.; Abrashev, M. V.; Popov, V. N.; Hadjiev, V. G. *Phys. Rev. B* **2003**, *67*, 212301.
(27) Podobedov, V. B.; Weber, A.; Romero, D. B.; Rice, J. P.; Drew, H. D. *Phys. Rev. B* **1998**, *58*, 43.
(28) Gayathri, N.; Raychaudhuri, K.; Tiwary, S. K. *Phys. Rev. B* **1997**, *56*, 1345.
(29) Croft, M.; Sill, D.; Greenblatt, M.; Lee, C.; Cheong, S.-W.; Ramanujachary, K. V.; Tran, D. *Phys. Rev. B* **1997**, *55*, 8726.
(30) Zeng, Z.; Greenbaltt, M.; Croft, M. *Phys. Rev. B* **1999**, *59*, 8784.
(31) Ignatov, A. Yu.; Ali, N.; Khalid, S. *Phys. Rev. B* **2001**, *63*, 014413-1.
(32) Bondino, F.; Plate, M.; Zangrando, M.; Zacchigna, M.; Cocco, D.; Comin, A.; Alessandri, I.; Malavasi, L.; Parmigiani, F. *J. Phys. Chem. B* **2004**, *108*, 4018.
(33) Ghgna, P.; Carollo, A.; Flor, G.; Malavasi, L.; Peruga, G. S. *J. Phys. Chem. B* **2005**, *109*, 4365.
(34) Kitayama, K.; Kobayashi, M.; Takano. H.; Nambu, N.; Hirasawa, H. *J. Solid State Chem.* **2003**, *176*, 151.
(35) Troyanchuk, I. O.; Szymczak, H.; Samsonenko, N. V.; Nabialek, A. *Phys. Status Solidi A* **1996**, *157*, 167.
(36) Bean, C. P.; Livingston, J. D. *J. Appl. Phys.* **1959**, *30*, 120S.